Mineralogical and microstructural characterization of biomass ash binder

Mineralogical and Microstructural Characterization of Biomass Ash Binder

Piyush Chaunsali[1], Hugo Uvegi[1], Rachel Osmundsen[1], Michael Laracy[2], Thomas Poinot[2], John Ochsendorf[2] and Elsa Olivetti[1]
[1]Department of Materials Science and Engineering, MIT, Cambridge, USA
[2]Department of Civil and Environmental Engineering, MIT, Cambridge, USA

Abstract

While the incineration of biomass residues is gaining traction as a globally available source of renewable energy, the resulting ash is often landfilled, resulting in the disposal of what could otherwise be used in value-added products. This research focuses on the beneficial use of predominantly rice husk and sugarcane bagasse-based mixed biomass ashes, obtained from two paper mills in northern India. A cementitious binder was formulated from biomass ash, clay, and hydrated lime (70:20:10 by mass, respectively) using 2M NaOH solution at a liquid-to-solid mass ratio of 0.40. Compressive strength of the biomass ash binder increased linearly with compaction pressure, indicating the role of packing density. Between the two mixed biomass ashes used in this study, the one with higher amorphous content resulted in a binder with higher strength and denser reaction product. Multi-faceted characterization of the biomass ash binder indicated the presence of aluminum-substituted calcium silicate hydrate, mainly derived from the pozzolanic reaction.

Keywords: Biomass ash; Clay; Characterization; Pozzolanicity; Alkali-Activation; Amorphous content

Introduction

Biomass residues, rich in carbon due to their biogenic nature, have long been one of the most heavily utilized energy sources and are often consumed alongside coal and other fossil fuels as a feedstock for powering industry. Primary solid biofuels (i.e., plant matter used directly as fuel or converted into solid fuels) are responsible for approximately 9% of global energy production, while they play an even larger role in developing countries, contributing as much as 35% of total energy generation [1,2]. Though traditional uses of biomass, such as in-home burning for heat, are not expected to grow significantly, large-scale industrial biomass incineration for combined heat and power is predicted to triple by 2035, compared with 2008 levels [3]. This expansion is triggered, in part, by regulations touting biomass as a renewable source of energy and its combustion, a CO_2-neutral process [4–6]. While effective as a method of converting waste to energy, combustion often results in significant ash production due to the complex chemical makeup of many feedstocks. The incineration process generally does not consume inorganic constituents, which remain as ash along with a percentage of unburnt carbon, dependent on process temperature and efficiency [7,8].

Agricultural residues, a subset of biomass residue that includes straws, husks, and woods, have been studied by an array of disciplines due to their global prevalence and wide-ranging chemical compositions. The focus of soil and fuel scientists alike, agricultural residues have more recently received the attention of the cement industry and those interested in lower-emission alternatives. While the inorganic content of these residues is initially low, pre-combustion inorganic phases translate reliably to post-combustion ash composition. Therefore, materials such as rice husk ash (RHA) and sugarcane bagasse ash (SCBA) are gaining increasing attention due to their relatively high concentrations of silica (SiO_2), a compound vital to many industrial applications, including

the production of concrete and its lower energy alternatives, geopolymers, and alkali-activated materials (AAMs) [9–11].

Consequently, the number of studies exploring the pozzolanic activity of biomass ashes has seen a steady uptick in recent years. These investigations have examined ash as a supplementary cementitious material, resulting in systems primarily composed of ordinary Portland cement (OPC) [12]. Alkali-activated and geopolymeric systems [13–16] aim to decrease the use of conventional OPC, and have the potential to do so with significantly lower environmental impact than predominantly OPC systems [17]. With increasing interest in environmental sustainability and the reduction of greenhouse gas emissions, there has been a large push for the cement and concrete industries to reduce their carbon footprint, which, by some estimates, ranges from 5-7% of global annual CO_2 emissions [18,19]. The advent of these alternatives reflects and advances this development, especially through the beneficial use and up-cycling of industrial byproducts and waste materials such as biomass ashes.

While a number of studies have examined the chemical compositions of biomass residues and their ashes, few have done so with the expressed interest of their applicability to alkali-activated systems as we do in this study [20,21]. Biomass ashes have been found to be extraordinarily variable systems, with an array of physical and chemical properties often related to their original biological functions [7,22]. RHA and SCBA are of particular interest in this study due to their high silica content. With reported levels of SiO_2 in ranging from 65–95%, and global production exceeding 30 million metric tons annually [23-26], they are prime candidates for use in both alkali-aluminosilicate and calcium silicate hydrate systems. Through their dissolution in basic media, ashes such as these have been shown to contribute much of their silicon to the formation of networked inorganic polymer and hydration products. The rate of this dissolution is highly

dependent on the choice and concentration of solvent and is essential to the formation of strongly networked products [27].

Silica content alone, however, does not render these ashes useful. Combustion temperature of the original agricultural residues is an important determinant of ash reactivity, as it often directly impacts both the particle size and crystallinity of the resulting ashes [28,29]. For alkali-activated systems, high surface area, amorphous particles are known to be the most highly reactive. While high incineration temperatures can often result in smaller particles, they also tend to crystallize inorganic constituents, thereby diminishing particle reactivity [28–30]. Mechanical activation of ashes can also have a beneficial impact on reactivity, as activation directly increases particle surface area [31, 32].

In this study, we explore the suitability of mixed biomass ash (composed predominantly of RHA and SCBA) as the primary component in a novel binding material. Motivated by challenges we have observed first hand in India, our focus has been the development of a product which simultaneously reduces the environmental impacts associated with this often-landfilled industrial byproduct and decreases the reliance on conventional topsoil-clay sourced bricks—a product which would have broader impact across the developing world. Collaboration with paper mills in northern India has allowed for the investigation of mixed-feedstock ashes in the pursuit of these goals.

Current work focuses on a detailed mineralogical and morphological characterization of both reactants and binder products resulting from alkali-activation of biomass ash. Earlier efforts by a subset of the authors aimed to establish a robust formulation capable of incorporating various ashes in a sustainable masonry product [33]. Where much of the literature has emphasized the use of coal fly ash as a precursor for AAMs, this paper examines the influence of physico-

chemical characteristics of biomass ash on the evolution of mineralogy, microstructure, and properties of alkali-activated biomass ash binders. Furthermore, while some studies have examined the effects of ash pretreatment on reactivity, we make an effort to utilize as-received ashes in an attempt to minimize environmental burden and cost. The biomass ash used in this study exhibited similar compositional characteristics to those reported in previous studies [7,24]. By reacting industrially-sourced biomass ash, locally available clay, and hydrated lime in aqueous sodium hydroxide solution, this work exploits the pozzolanic nature of these precursors through alkali activation to further scientific understanding of a yet unexplored system.

Experimental Program

Materials

In this study, two ashes were used, sourced from Bindlas and Silverton Paper Mills in Muzaffarnagar, Uttar Pradesh, India. Bindlas ash was reported as the byproduct of 63% sugarcane bagasse, 27% rice husk, and 10% petroleum coke, whereas Silverton ash was reported to be the byproduct of 70–100% rice husk, with the balance composed of sugarcane bagasse. While petroleum coke was included as a feedstock at Bindlas Paper Mill, it is known to produce <1% ash [34], and was thus assumed to have minimal impact on the final composition of bottom ash. Therefore, the current study focuses on the bio-based components, and a future study could include the constituents derived from petroleum coke. Due to the variable and mixed nature of the residue feedstock, these ashes are typically landfilled. In an attempt to maintain local sourcing of materials, these ashes were mixed with Indo-Gangetic clay—the same used for local fired clay brick production—as well as hydrated lime (calcium hydroxide) and sodium hydroxide, both of which are already heavily used by these partners in the paper industry. Table 1 shows the oxide composition of the raw ashes and clay. The ashes were found to be

predominantly siliceous, with alumina content lower than 3% and an array of other oxides. As shown in Table 2, phase composition of the ashes indicates the presence of phases such as quartz, albite, cristobalite, sylvite, and arcanite. The amorphous content in Silverton ash was higher than in Bindlas ash, while the clay was significantly more crystalline than either ash investigated. It is important to note that a part of the amorphous content in both ashes is due to the presence of unburnt carbon. The clay had relatively lower amorphous content (~20%) compared to biomass ashes whose amorphous content ranged from 85–91%. Between the two ashes, Bindlas ash had a higher loss on ignition (LOI) indicating a greater presence of unburnt carbon. Clay reported ~3.4% loss-on-ignition which was mainly derived from the dehydroxylation of clinochlore and muscovite phases. Specific surface area was also higher for Bindlas ash than for Silverton ash (Fig. 1 (a)). As unburnt, activated carbon typically exhibits high surface area, this similarly indicated higher unburnt carbon content in Bindlas ash, in agreement with findings previously reported by Yeboah et al. [22]. Silverton ash had a marginally finer average particle size than Bindlas ash (Fig. 1 (b)), with respective mean particle sizes of ~170 μm and ~120 μm. Ashes were sieved to obtain particles less than 500 μm in size, but since the goal was to utilize ashes as received, no mechanical grinding was performed. Scanning electron micrographs of both ashes show highly porous morphology (Figs. 1 (c) & (d)).

Table 1. Oxide composition of raw materials (wt. %, dry basis)

Element as Oxide (wt. %)	Bindlas Ash	Silverton Ash	Clay
SiO_2	55.00	61.33	71.70
Al_2O_3	2.43	1.30	13.30
Fe_2O_3	0.94	0.68	5.03
SO_3	1.29	1.74	0.02
CaO	1.06	1.51	0.77
Na_2O	0.35	0.13	0.96
MgO	0.75	0.70	1.51
K_2O	2.21	2.30	2.53
P_2O_5	0.67	0.85	0.07
TiO_2	0.13	0.08	0.59
MnO_2	0.06	0.08	0.10
BaO	0.01	0.01	0.05
SrO	0.01	0.01	0.01
Loss on Ignition (750°C)	35.07	29.28	3.37

Table 2. Phase composition of raw materials (wt. %)

Element as Oxide (wt. %)	Bindlas Ash	Silverton Ash	Clay
Albite	0.8	0.7	5.9
Quartz	13.4	4.3	48.8
Cristobalite	--	0.5	--
Sylvite	--	1.0	--
Arcanite	--	1.8	--
Anorthoclase	0.6	--	--
Calcite	--	0.3	--
Muscovite	--	--	14.4
Microcline	--	--	4.7
Clinochlore	--	--	3.3
Fluorophlogopite	--	--	2.3
Kaolinite	--	--	0.6
Amorphous Content*	85.2	91.4	19.8

*Determined using quantitative X–ray diffraction analysis

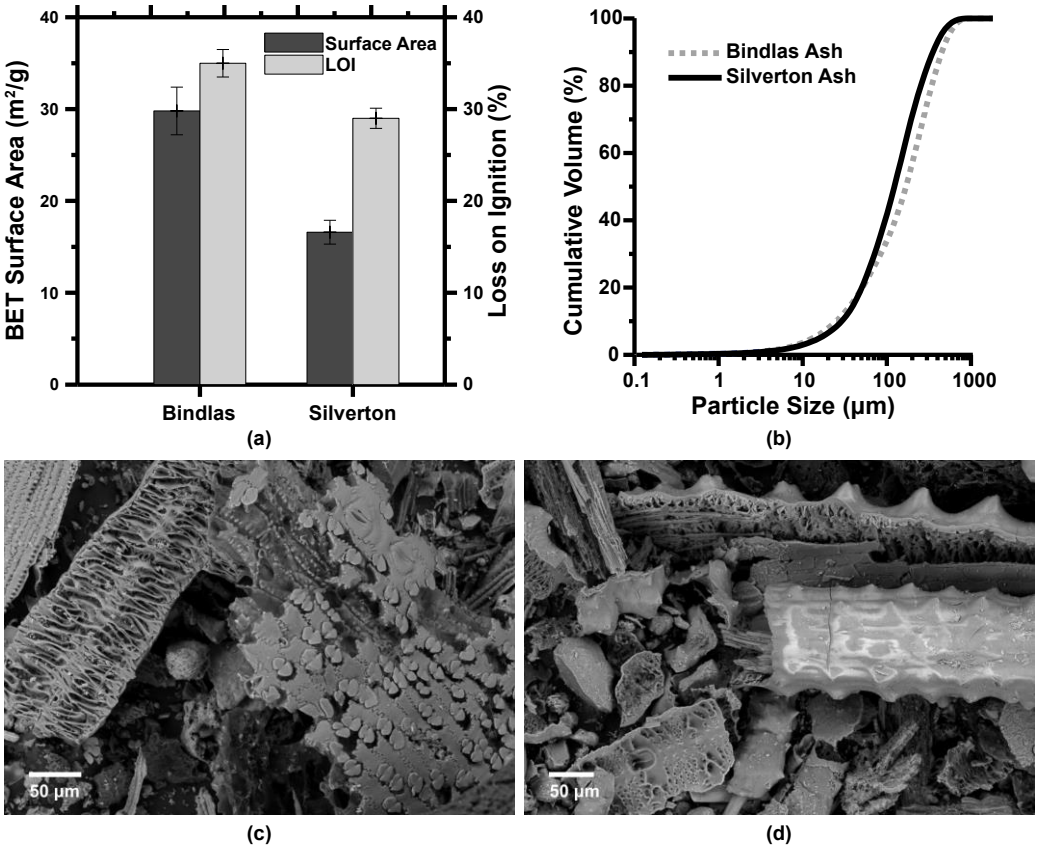

Figure 1. Raw material characterization of ashes: (a) specific surface area and loss on ignition, (b) particle size distribution, (c) – (d) scanning electron micrographs of Bindlas and Silverton ashes, respectively

Methods

Sample Preparation

As the ash is typically landfilled by the source partners, samples were prepared with the goal of maximizing the use of biomass ash. Clay was added as a stabilizing material, whereas hydrated lime was added as a source of calcium to increase sample strength. Biomass ash, clay, and hydrated lime were proportioned (by wt.) at 70%, 20%, and 10%, respectively. This mixture proportion attained the maximum strength among the various combinations of ash, clay, and lime, and therefore, was chosen for this study. This proportion was fixed for different ashes to assess the robustness of formulation. More details on the mixture proportion development can

be found in Laracy et al. [33]. The homogenized dry powder of biomass ash, clay, and lime was mixed with 2M NaOH solution at a liquid-to-solid mass ratio of 0.40 for all mixtures. The activating solution (i.e. 2M NaOH) was prepared by dissolving NaOH pellets (Macron Fine Chemicals, ≥98% assay) in de-ionized water. The mixing was performed in a Kitchen Aid mixture at the maximum speed (~220 rpm) for 15 minutes. Samples were then hydraulically pressed into 200 gram cubes, compacted using a Baldwin Tate Emery Universal Testing Machine to final pressures of 10, 15, 20, 25 and 30 MPa with a fixed loading rate of 15000 N/min. The compaction mold had inner dimensions of 50 mm × 50 mm × 150 mm. The compacted samples were measured to have a base of approximately 50 mm × 50 mm with height varying from 44–50 mm depending on the compaction pressure. Subsequently, samples were wrapped in plastic sheet and stored in an oven operating at 30 °C ± 2°C until testing and characterization occurred. These experiments were performed on triplicates of samples at two different times to ensure the reproducibility of the results.

Compressive Strength

Compressive strengths of the compacted samples were determined after 1, 7, and 28 days. Samples were tested at a loading rate of 15000 N/min, the same as that used for compacting.

Inductively Coupled Plasma Optical Emission Spectrometry (ICP-OES)

An Agilent 5100 Vertical Dual View ICP-OES with an auto-sampler was used to analyze reactant dissolution. Calibration samples of 0.1 ppm, 1 ppm, 10 ppm, 50 ppm 100 ppm, 500 ppm, and 1000 ppm of Ca, Al, Si, Na, and K were prepared from a standard solution containing 1000 ppm of Ca, Al, Si, Na, and K elements (Elemental Scientific, Omaha, NE) using Milli-Q water (Millipore, ≥18 MΩ.cm) for dilution. The samples were prepared in 2% HNO_3 (TraceSELECT, Sigma-Aldrich).

Thermogravimetric Analysis (TGA)

Thermogravimetric analysis was performed to determine the bound water content of reaction product on 25 ± 2 mg of powdered samples passing through 40 μm size sieve using a Q50-TA Instrument. The samples were heated in a nitrogen environment (flow: 50 ml/min) up to 900 °C at a rate of 15°C per minute.

X-ray Diffraction (XRD)

Mineralogical phase distributions of raw materials and hydrated samples were determined using X-ray diffraction. Samples were crushed, immersed in isopropyl alcohol, filtered, and finally dried under vacuum, before further milling and sieving to a fine powder (<45 μm). XRD data was collected using high speed Bragg-Brentano optics on a PANalytical X'Pert Pro MPD operated at 45 kV and 40 mA. Data was obtained between 5° and 70° (2θ) using a step size of 0.0167° with each sample scan lasting 52 minutes. The diffractometer was configured with a 1/2° divergent slit, a 0.04 radian soller slit, and a 1° anti-scatter slit. The powdered sample was packed into a 27 mm diameter sample holder. HighScore Plus software was used for quantitative X-ray diffraction (QXRD) using Rietveld analysis [35]. The refined parameters included phase scale factors, background coefficients, zero-shift error, lattice parameters, peak shape parameters, and preferred orientation, if needed. An internal standard method based on the addition of corundum (Al_2O_3) was employed to quantify amorphous content, varying internal standard content at 10%, 15%, and 20% to check the consistency of Rietveld XRD results. After verification of consistency, a 15% internal standard was used in all further tests.

Fourier Transform Infrared Spectroscopy (FTIR)

FTIR Spectroscopy was performed using a Thermo Scientific Nicolet 6700 Fourier Transform Infrared Spectrometer. Transmission spectra were collected from 4000 to 400 cm^{-1} with a

resolution of 2 cm^{-1}. Spectra were averaged over 32 scans. Samples were run using the KBr pellet method, with approximately 1mg of sample blended with 400mg of KBr matrix immediately prior to measurement. Samples were dried, milled, and sieved as described in the XRD method above. To ensure reproducibility of results, 6 different pellets were prepared for each sample type.

Nitrogen Sorption Test

Nitrogen adsorption and desorption isotherms were measured at 77 K on a Micromeritics ASAP 2010 system. Before the measurement, samples were degassed at 50 °C under vacuum for several hours. The surface area of the samples was calculated by the Brunauer-Emmet-Teller (BET) theory. The Barrett-Joyner-Halenda (BJH) theory was used to evaluate the pore size distribution from the adsorption isotherm.

Scanning Electron Microscopy (SEM) and Energy Dispersive X-Ray Spectroscopy (EDS)

For microscopy, samples were cut using a low-speed diamond saw and were subsequently immersed in isopropanol for 24 hours before vacuum drying for another 24 hours. The dried samples were impregnated with epoxy (EpoThin 2.0, Buehler) in a vacuum desiccator. Upon hardening, samples were ground and polished using silicon carbide papers and Struers diamond pads down to a 1 μm diamond suspension. All samples were sputter coated with gold to minimize surface charging during microscopy. A Zeiss Merlin High Resolution Scanning Electron Microscope equipped with an in-lens detector, a retractable 4 Quads backscatter detector, and an EDAX detector was used for SEM and EDS.

Results and Discussion

With the goal of mineralogical and microstructural characterization of alkali-activated biomass ash binders, this section contributes to the understanding of raw material (i.e., ash and clay)

reactivity, mineralogical and microstructure evolution, and strength development of biomass ash binders. By combining the results from three sub-sections on: 1) reactivity of raw materials, 2) strength development and phase composition, and 3) microstructure characterization, the properties of biomass ash binders are discussed.

Reactivity of Raw Materials

Reactivity of raw materials such as biomass ash and clay is expected to have a direct influence on the property development of the resulting binder. A previous study by He et al. [36] compared the properties of binders derived from alkali-activation of metakaolin and red mud-fly ash. They reported that the metakaolin binder exhibited higher strength than red mud-fly ash binder due to higher reactivity of metakaolin. As a measure of reactivity in this work, amorphous content was determined using QXRD analysis. Amorphous content was evidenced by an amorphous hump between 15°and 30° (2θ) in XRD patterns (Fig. 2 (a)). QXRD showed Silverton ash to have higher amorphous content (~91%) than Bindlas ash (~85%). The high amorphous content of the ashes used in this study is partly due to the presence of unburnt carbon, also exhibited by high LOI value. In order to determine the reactive amorphous aluminosilicate phase, Bindlas and Silverton ashes were calcined at 500 °C for 3 hours to remove the unburnt carbon. The QXRD of the calcined ashes showed ~ 73% and ~89% for Bindlas and Silverton ashes, respectively. The difference in the amorphous contents of both ashes is more pronounced after calcination. Therefore, for ashes with high LOI, the degree of amorphousness must be evaluated after accounting for the unburnt carbon.

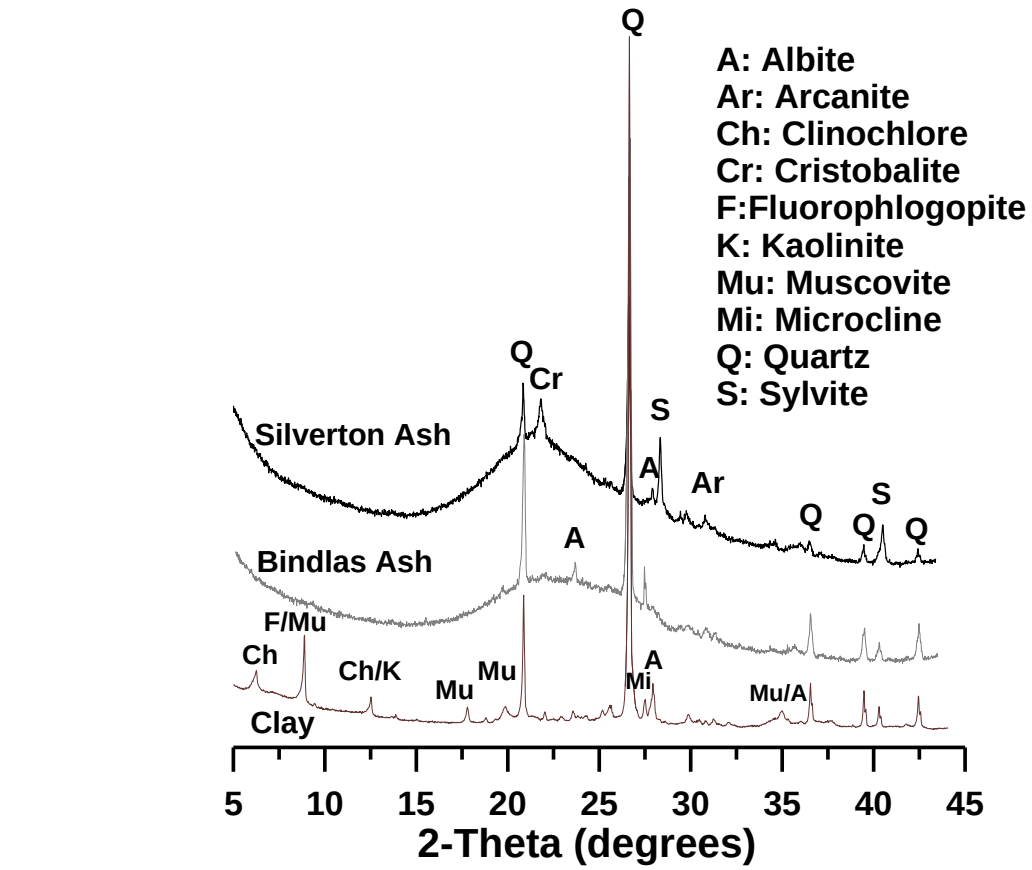
A: Albite
Ar: Arcanite
Ch: Clinochlore
Cr: Cristobalite
F:Fluorophlogopite
K: Kaolinite
Mu: Muscovite
Mi: Microcline
Q: Quartz
S: Sylvite
Silverton Ash
Bindlas Ash
Clay
Q
Cr
S
A
Ar
F/Mu
Ch
Ch/K
Mu
Mi
Mu/A
5
10
15
20
25
30
35
40
45
2-Theta (degrees)

(a)

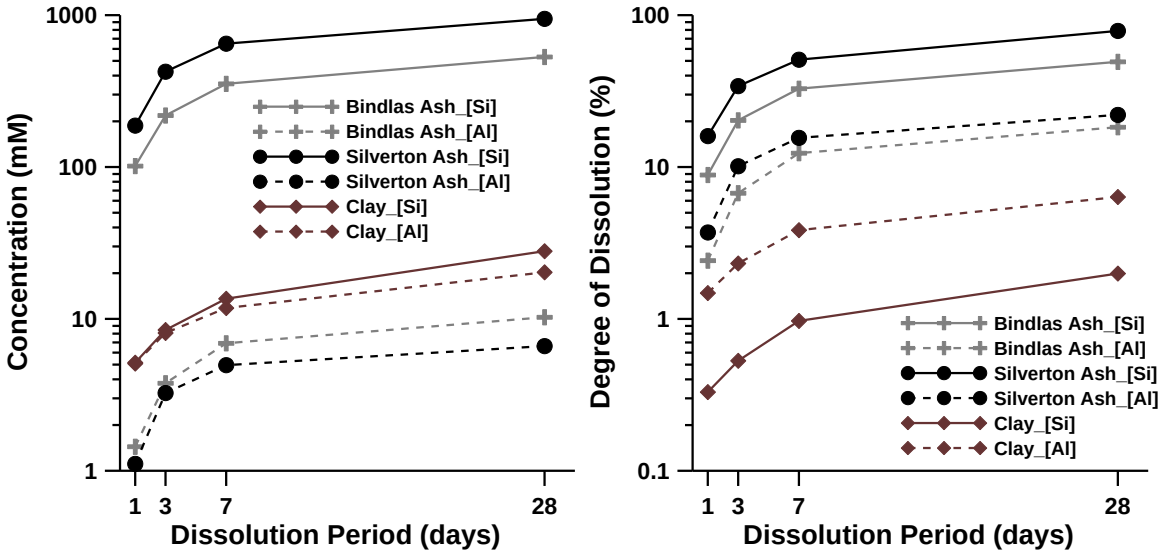
Concentration (mM)
1000
100
10
1
Bindlas Ash_[Si]
Bindlas Ash_[Al]
Silverton Ash_[Si]
Silverton Ash_[Al]
Clay_[Si]
Clay_[Al]
1
3
7
28
Dissolution Period (days)
Degree of Dissolution (%)
100
10
1
0.1
Bindlas Ash_[Si]
Bindlas Ash_[Al]
Silverton Ash_[Si]
Silverton Ash_[Al]
Clay_[Si]
Clay_[Al]
1
3
7
28
Dissolution Period (days)

(b) (c)

Figure 2 (a) X-ray diffraction patterns of raw materials, (b) dissolved aluminum [Al] and silicon [Si] elements using ICP-OES, and (c) degree of dissolution of ash and clay in 2M NaOH solution

Reactivities of the raw materials in the context of the described formulation were also assessed by monitoring their dissolution in 2M NaOH solution. Examining the dissolution of amorphous aluminosilicate precursors is essential to understanding and controlling the behavior of resulting binders. Previous studies have shown that the dissolution rate of aluminosilicate precursors such as kaolinite and muscovite depends on the pH, temperature, aqueous [Al] concentration and chemical affinity [37]. In this study, dissolution of individual raw material was monitored in 2M NaOH (pH ~ 13.8) aqueous solution. Various samples were prepared by adding 1 g of raw material into 10 ml of 2M NaOH solution. At progressive ages, the solution was vacuum filtered using 0.2 μm filter paper. Subsequently, an aliquot of filtered solution was used for ICP-OES analysis as described in the *Methods* section. Figure 2 (b) shows the dissolved [Al] and [Si] from ashes and clay at various ages. The concentrations of dissolved [Al] and [Si] increased with time for all samples tested. Furthermore, both ashes released significantly larger amounts of [Si] into solution than did the clay, potentially due to their higher amorphous content. Interestingly, clay released similar levels of [Al] and [Si] into the solution. Hajimohammadi and van Deventer [27] examined the dissolution behavior of various silicate and aluminosilicate sources and reported that the dissolution rates of silicate sources (i.e., rice husk ash and geothermal silica) were much higher than the aluminosilicates (i.e., fly ash, slag and metakaolin). They also reported that the dissolution rates of [Si] and [Al] species were similar in fly ash and slag systems which draws similarity to the results of clay dissolution in our study. Between the two ashes, Silverton ash released more [Si] and less [Al] than did Bindlas ash. By looking at the oxide composition of both ashes, it becomes evident that Bindlas had higher alumina than Silverton ash, thereby

explaining the trend in dissolved [Al]. To explain the difference in levels of dissolved [Si] from each ash, we connect this result to the relative amorphous content. As Silverton ash had higher amorphous content than did Bindlas ash, the [Si] from Silverton ash more readily dissolved in the NaOH solution. Continuous dissolution was demonstrated by the significant increase in concentration of both [Si] and [Al] concentrations in solution from 1 to 7 days and continued increases from 7 to 28 days. This information can be further understood through the examination of degree of dissolution. Degree of dissolution of raw materials was calculated from the ratio of dissolved element (from ICP) to total elemental presence (from XRF). Figure 2 (c) shows that the Silverton ash had a higher degree of dissolution than Bindlas ash at all ages. After 28 days, ~49% of [Si] and ~18% of [Al] were dissolved from Bindlas ash, whereas Silverton ash reported ~79% of [Si] and ~22% of [Al] dissolution. The clay used in this study exhibited ~2% [Si] and ~6% [Al] dissolution at the end of 28 days, indicating its lower reactivity. Therefore, it appears that the clay is acting more as a filler than a source of alumina.

Amorphous content and particle dissolution rates provide an early insight into the extent of precursor reactivity. Although the ICP study was carried out in environments more dilute than the system being studied (i.e., 1 g solid in 10 ml of activator as compared to 1 g solid (ash/clay/lime) in 0.4 g of activator), the results are useful for comparing reactivities of the biomass ashes and clay. Furthermore, the results set an upper bound on in-situ elemental availability, as the reaction process involves competition between dissolution of reactants and precipitation of products. Preliminary work exploring the simultaneous nature of reactant dissolution and product formation has demonstrated relatively lower levels of both [Si] and [Al] in solution when samples are prepared with the formulation specific solid ratio (70/20/10) and dissolution study liquid-to-solid ratio (10 ml/1 g). Further investigation is needed to examine the

dissolution kinetics of individual constituents (crystalline and amorphous phases) of biomass ash and its relationship to strength development of biomass ash binders.

Strength Development and Phase Composition

Compressive strengths of compacted samples were determined after 7 days of curing for the following initial compaction pressures: 10, 15, 20, 25, and 30 MPa, as shown in Fig. 3 (a). With increased compaction pressure, compressive strengths exhibited a steady increase. Using this compaction pressure-strength relationship, compressive strength can be manipulated to achieve performance targets by modifying the packing density. The Silverton ash binder exhibited higher strength than the Bindlas ash binder at all compaction pressures. The effect of compaction pressure was studied to simulate the industrial brick-making process where the pressure can vary noticeably. After examining the role of pressures in range of 10–30 MPa, the study only focused on 10 MPa, as it provided the lower bound of a desired pressure level for attaining the required strength within 7 days of curing. Figure 3 (b) shows the evolution of compressive strength at 1, 7 and 28 days for the samples compacted at 10 MPa. Mirroring the aforementioned relationship between the two ash binders, the compressive strength of Silverton ash binder was higher than that of Bindlas ash binder at all ages. We note that approximately 50% of the 28-day strength was achieved in first 24 hours of curing. Higher amorphous content of raw Silverton ash, therefore, appears to be the governing factor behind the higher strength of Silverton ash binders as compared to Bindlas ash binders.

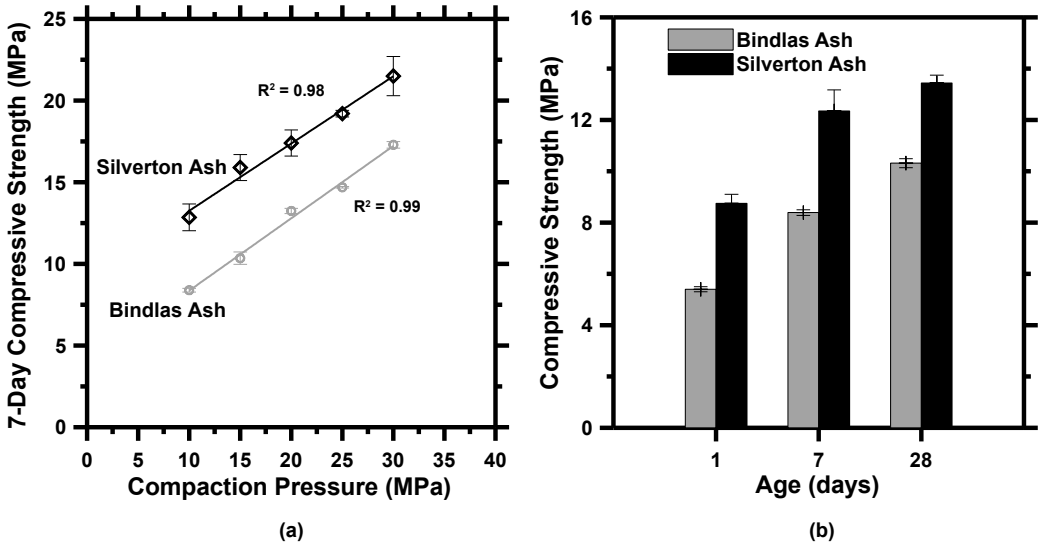

Figure 3 (a) Influence of compaction pressure on 7-day strength, and b) Influence of curing duration on strength of samples prepared at compaction pressure of 10 MPa

Hydration progress of the biomass ash binders was monitored using XRD, which shows the evolution of phases with time. Figures 4 (a) and (b) compare the XRD patterns of raw ash, clay, and binders (age: 1 and 28 days). Most peaks from the unreacted ash and the clay were evident in both biomass ash binders. A new peak around 29.2° (2-theta) appeared in both binders after 1 day of curing, indicating the presence of a calcium-silicate-hydrate phase (abbreviated as C-S-H) [38,39]. Since the calcite phase also has its strongest peak at 29.4° (2-Theta), it was important to assess the extent of carbonation. As will be discussed in TGA results, the extent of carbonation was very low (i.e., ~1.4% of dry mass) in biomass ash binders. Moreover, the samples were wrapped in plastic sheet during curing, and stored in desiccator during drying to prevent carbonation. The formulation used in this study can be compared to alkali-activated slag or alkali-activated fly ash-slag systems. In alkali-activated slag systems, C-S-H has been found to be the major hydration product [40–43]. Furthermore, Ismail et al. [43] reported the presence of aluminum substituted C-S-H phase in alkali-activated fly ash-slag systems with more than 50%

slag. The composition of calcium silicate hydrate can vary significantly based on the calcium content of the starting material. The C-S-H present in ordinary Portland cement systems has Ca/Si ratio in the range of 1.5–1.9 [44]. The C-S-H in systems containing supplementary cementitious materials such as fly ash, silica fume, slag, and metakaolin differs from the C-S-H in Portland cement, with the Ca/Si ratio (molar) of blended cement systems typically lower than in Portland cement. The XRD peak position at around 29.2° (2-theta) has been shown to be unaltered by the variation in Ca/Si ratio [45,46]. Due to low calcium (10% lime) content in starting formulation (70% ash, 20% clay and 10% hydrated lime), the C-S-H phase present in the biomass ash binder is expected to have a low Ca/Si ratio. As shown in Fig. 2 (b), [Al] and [Si] concentration increased with time, leading to an increase in C-S-H formation. The availability of [Al] in solution will also lead to its incorporation in C-S-H phase [47]. Increase in strength from 1 day to 28 days is possibly due to continuous dissolution of [Al] and [Si] from ash and clay and the formation of C-S-H phase in the presence of [Ca] originating from hydrated lime. Based on XRD patterns, C-S-H appears to be the main reaction product in biomass ash binders. We note that that the presence sodium aluminosilicate cannot be completely dismissed as it may co-exist with calcium silicate hydrate phase. Still, in the context of the dissolution data, C-S-H with low Ca/Si ratio is likely the most prevalent product. We also note the disappearance of the sylvite phase originally present in the Silverton ash upon dissolution in NaOH, as there was no peak corresponding to sylvite in the Silverton ash binder.

Quantitative X-ray diffraction (QXRD) analysis was carried out to estimate the amorphous content of biomass ash binders. QXRD indicated higher amorphous content in Silverton ash binders than in Bindlas ash binders (Fig. 4 (c)). Binder amorphous content derives from a combination of amorphous material found in the ash and clay in addition to formation of C-S-H,

a semi-crystalline product. Amorphous content in the Silverton ash binder was 4–6% higher than in the Bindlas ash binder, which correlated well with the higher strength of Silverton ash binder. Although the amorphous content was not normalized with respect to initial unhydrated material or total paste content, a comparison between two binders can still be made from the results obtained on the dry powdered binders.

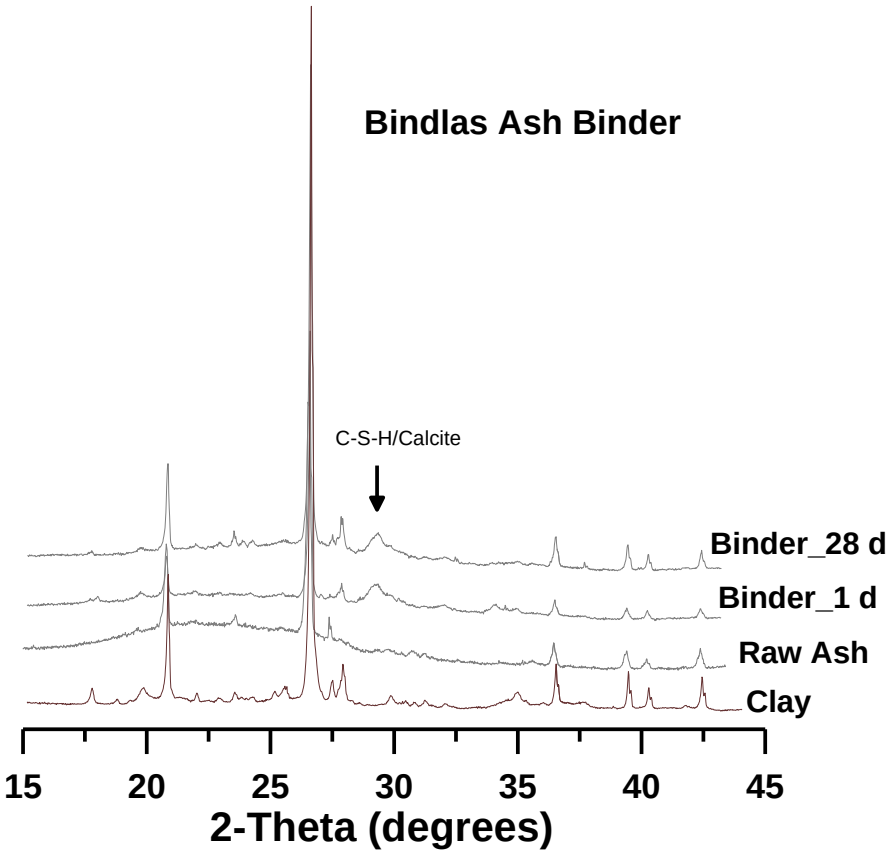

(a)

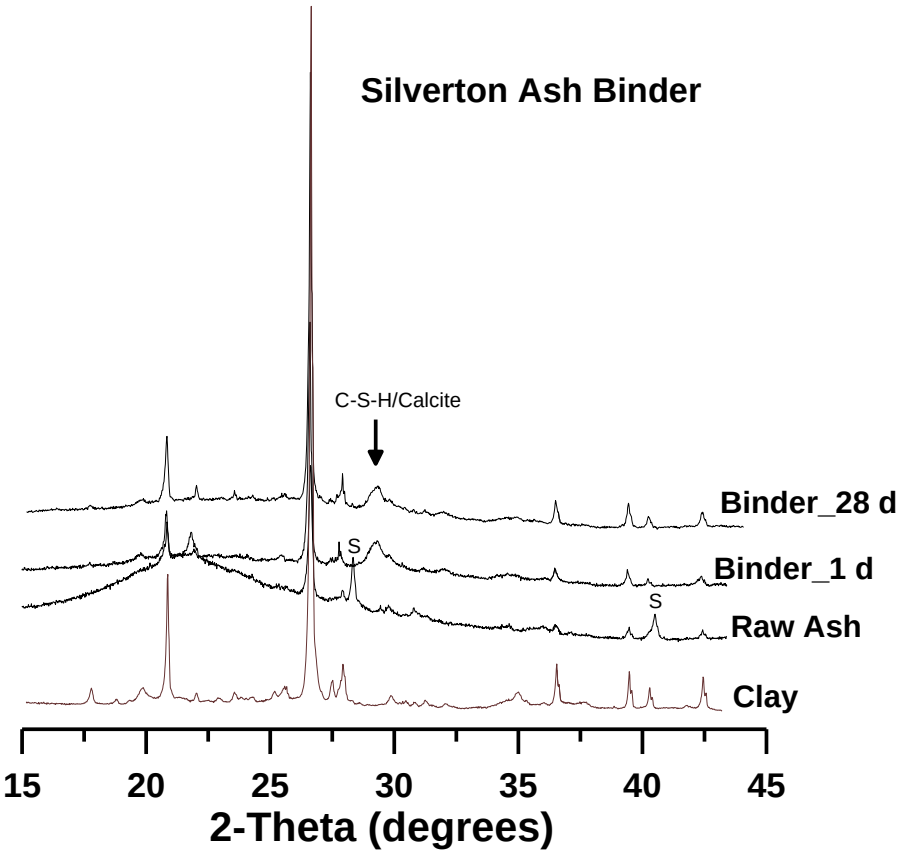
Silverton Ash Binder
C-S-H/Calcite
S
S
Binder_28 d
Binder_1 d
Raw Ash
Clay
15
20
25
30
35
40
45
2-Theta (degrees)

(b)

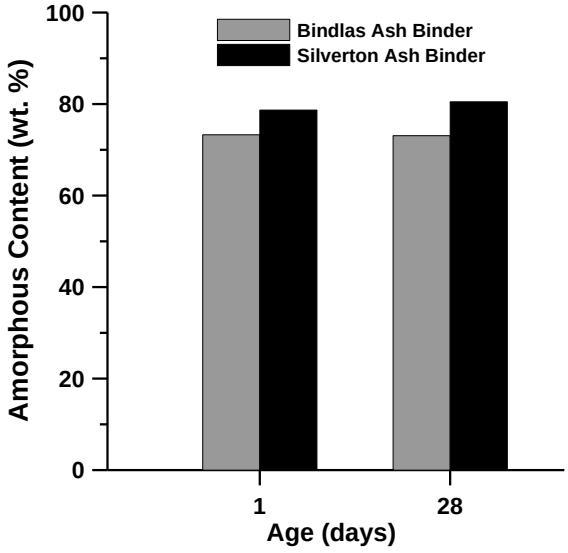
Bindlas Ash Binder
Silverton Ash Binder
Amorphous Content (wt. %)
0
20
40
60
80
100
1
28
Age (days)

(c)

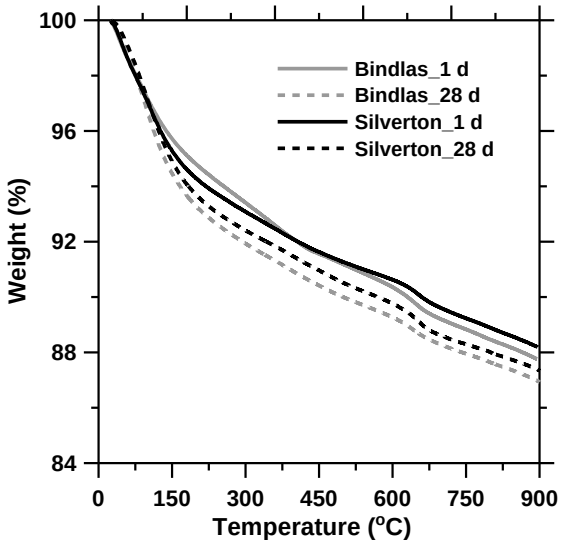
Bindlas_1 d
Bindlas_28 d
Silverton_1 d
Silverton_28 d
Weight (%)
84
88
92
96
100
0
150
300
450
600
750
900
Temperature (°C)

(d)

Figure 4 (a)-(b) Phase composition (C-S-H: calcium silicate hydrate; S: sylvite), (c) amorphous content, and (d) thermogravimetric analysis of biomass ash binders at various ages

Thermogravimetric analysis of the biomass ash binders (Fig. 4 (d)) showed an increase in weight loss between 1 and 28 days due to higher amount of reaction product (C-S-H) at 28 days. The C-S-H phase exhibits ~98% weight loss between 50 and 600°C due to the loss of structural water [44]. The weight loss between 50 and 600°C for biomass ash binders ranged from ~9–10% (of dry mass) for both binders which was ~75–80% of total weight loss in range of 22–900°C. Higher derivative weight at early stage (i.e., between 50 and 300°C) also indicates the loss of bound water from C-S-H phase. Although total weight loss is due in part to the presence of calcite and unreacted ash, the majority seems to have originated from the loss of bound water from C-S-H. It is noted that the weight loss of Bindlas and Silverton ash in the range of 22–900°C was reported to be ~5%. For both binders, the weight loss in range of 550–900°C was ~3% (of dry mass) which corresponds to ~1.4% calcite in dry binder. Therefore, the extent of carbonation was very low in the samples.

The reaction product of biomass ash binder was also characterized using FTIR spectroscopy. As shown in Fig. 5, a shoulder peak at ~965 cm^{-1} was observed in both binders. This peak location has been attributed to the presence of C-S-H phase [48]. Therefore, the FTIR result complemented the XRD finding which also highlighted the presence of C-S-H phase. Other peaks present in the range of 900–1100 cm^{-1} have been attributed to Si-O-T (T=Al,Si) as present in aluminosilicate type binders [48]. However, initial analysis accredits their occurrence to the presence of unreacted clay and ash material. Further investigation is still being conducted.

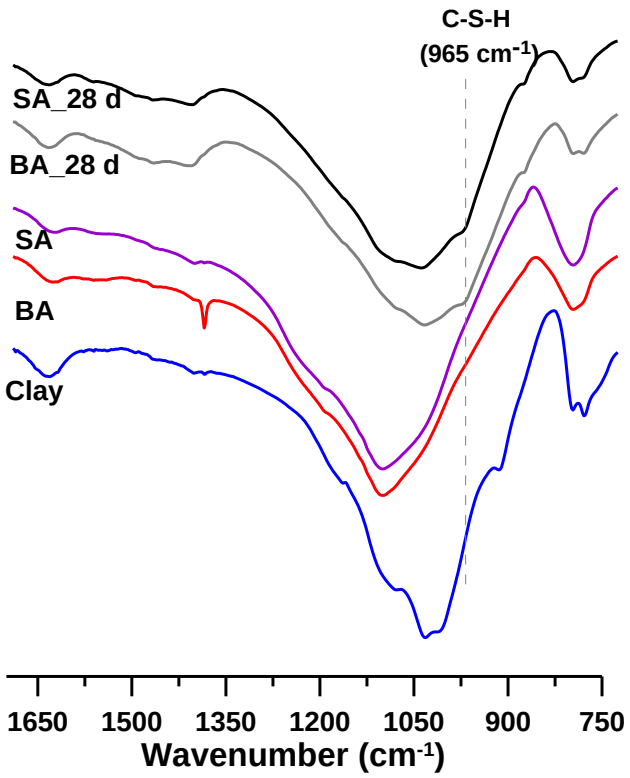

Figure 5. FTIR spectra of raw materials and 28-day old binders (Note: BA – Bindlas Ash; SA – Silverton Ash)

Nitrogen adsorption has been shown to capture changes in the microstructure of Portland cement and alkali activated binders [49,50]. The BET specific surface area of Silverton ash binders was higher than that of Bindlas ash binders (Fig. 6 (a)). Previous studies have shown that the specific surface area of Portland cement paste increases with time due to increased degree of hydration which results in higher amounts of C-S-H [49,51,52]. With increased C-S-H, there is also diminution of pore size, leading to higher surface area. The results presented in Fig. 6 were derived from small pieces of 1–2 mm thickness. In addition to bulk samples, powder samples (less than 45 μm size) were also analyzed. The influence of aging was consistent (specific surface area increased with aging) between bulk and powder samples. Although the difference

between the surface areas of Bindlas and Silverton ash binders was within 10%, the higher specific surface area of the Silverton ash binder can be related to its greater amorphous content.

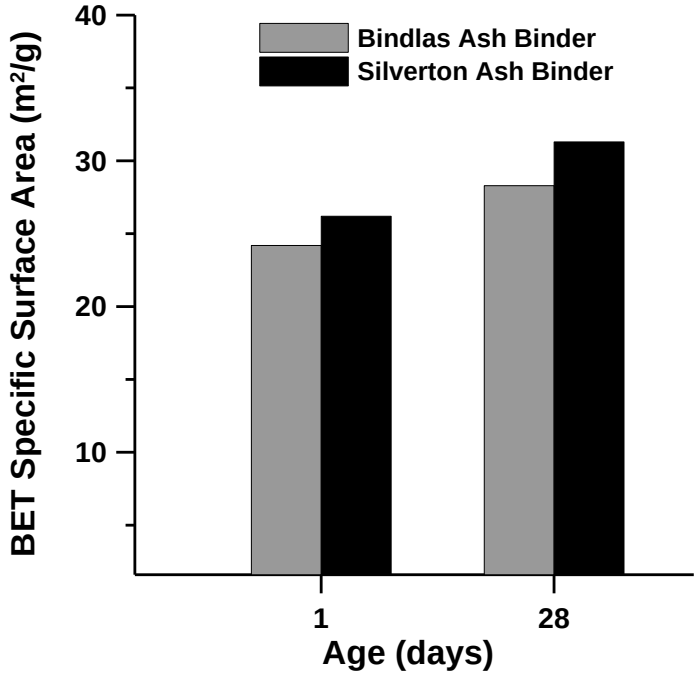

(a)

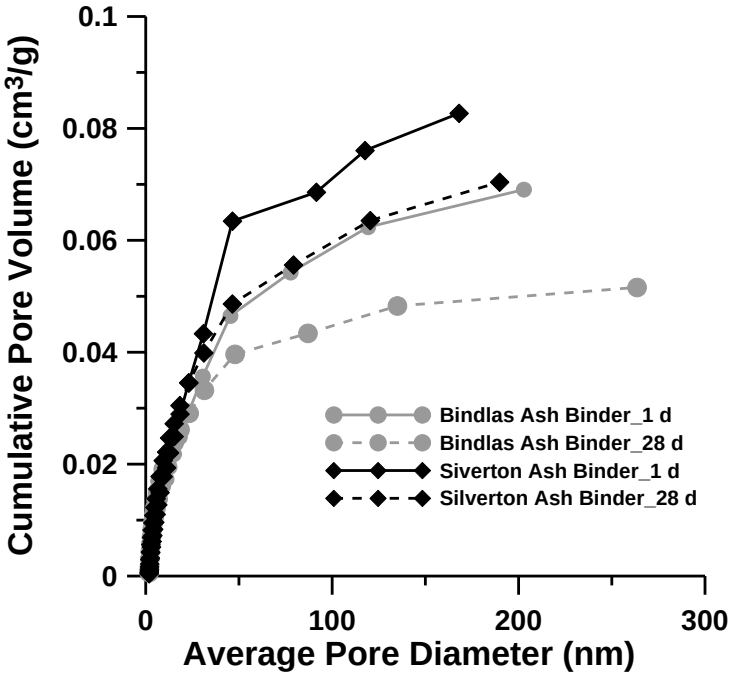

(b)

Figure 6 (a) BET specific surface area, (b) cumulative pore volume of biomass ash binders at 1 and 28 days

Figure 6 (b) shows the influence of curing (or aging) on pore structure characteristics of microstructure. We note that the BET test allows the measurement of pore sizes which are smaller than 300 nm. Even though BET does not capture the complete range of pore size, the changes in microstructure such as densification can be captured. As shown in Fig. 6 (b), the pore volume decreased with aging for both types of binders, indicating the densification of the microstructure.

Microstructure Characterization

Microstructural evolution of the binders was monitored using scanning electron microscopy (SEM) of polished samples. Figures 7 (a)–(d) show representative secondary electron (SE) micrographs of reaction product morphology evolution on sample surfaces after 1 and 28 days of curing. The binders exhibited a multi-scale and multi-phase structure as shown in a backscattered electron (BSE) micrograph in Fig. 7 (e), displaying a nanoporous reticulate structure binding larger micro- and meso-scale unreacted components. The globules observed in both systems are on the order of 10–50 nm in diameter, and interconnectedness of the globular network structure is observed to increase with age. Larger unreacted particles are visible throughout the samples, ranging on the order of ones to hundreds of microns in size. Particles that appear flat and lighter in color in the backscattered, low magnification image are primarily composed of silica, derived from both unreacted ash and clay, while areas that appear more intensely locally networked and darker are often rich in unburnt carbon. A SE image including a highly porous, carbonaceous region is presented in Fig. 7 (f). The pores in these regions are often on the order of ~10 μm. Reaction products have been observed to form on the carbon surfaces, although significantly less densely than in more siliceous regions of the samples.

Energy dispersive X-ray spectroscopy (EDS) data included in Fig. 8 indicate that the reaction product network is relatively homogeneous and composed primarily of C-S-H globules with moderate aluminum substitution. EDS data, therefore, confirms the presence of C-S-H phase found in XRD analysis. The Ca/Si ratio of the C-S-H present in Bindlas and Silverton ash binders varied in the range of 0.1–0.5. The reaction products of the Bindlas ash binder shown in Fig. 8 (a) have an apparent Ca/Si ratio in the range of 0.09–0.46 as indicated by phase composition of different colors in Fig. 8 (b). The Silverton ash binder products shown in Fig. 8 (c), on the other hand, exhibit a Ca/Si ratio in the range of 0.12–0.17 as indicated by phase composition map in Fig. 8 (d). Lower Ca/Si ratio of Silverton ash binder products may be due to the fact that higher amounts of [Si] released from Silverton ash than Bindlas ash resulted in lower Ca/Si ratio. Brough and Atkinson [41] examined the microstructure of alkali-activated slag and reported Ca/Si ratio in range of 0.5–1. Due to low calcium content in our starting formulation, the Ca/Si ratio of the resulting C-S-H appears to be lower than the reported values for the alkali-activated slag system. Although some studies have reported coexistence of a sodium aluminosilicate network and calcium aluminosilicate hydrate gel [43, 53], in this study, C-S-H with moderate aluminum substitution was found to be the dominant product present in biomass ash binders. The network is observed to densify with curing time, as corroborated by both BET measurements and micrograph images and as expected by the trend towards increased strength with sample aging. Despite their greater cumulative pore volume, reaction products in Silverton ash binders were observed to be more densely packed at all ages than those of Bindlas ash binders, further explaining the trends of compressive strength experiments.

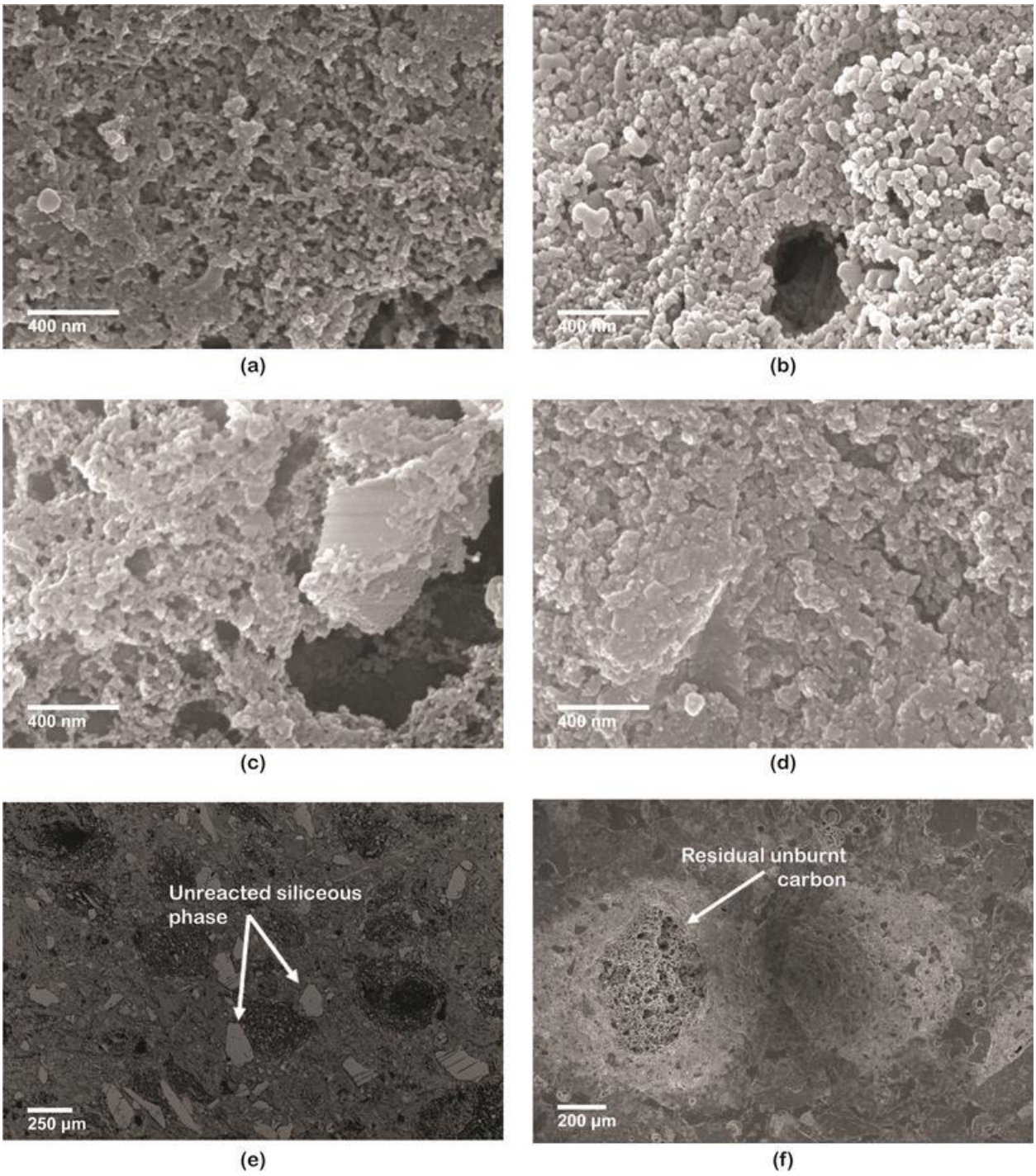

Figure 7 (a) – (b) SE micrographs of polished Bindlas ash binders at 1 and 28 days, (c) – (d) SE micrographs of polished Silverton ash binders at 1 and 28 days, (e) BSE micrograph of polished 7 day Bindlas ash binder, (f) SE micrograph including observed carbonaceous region

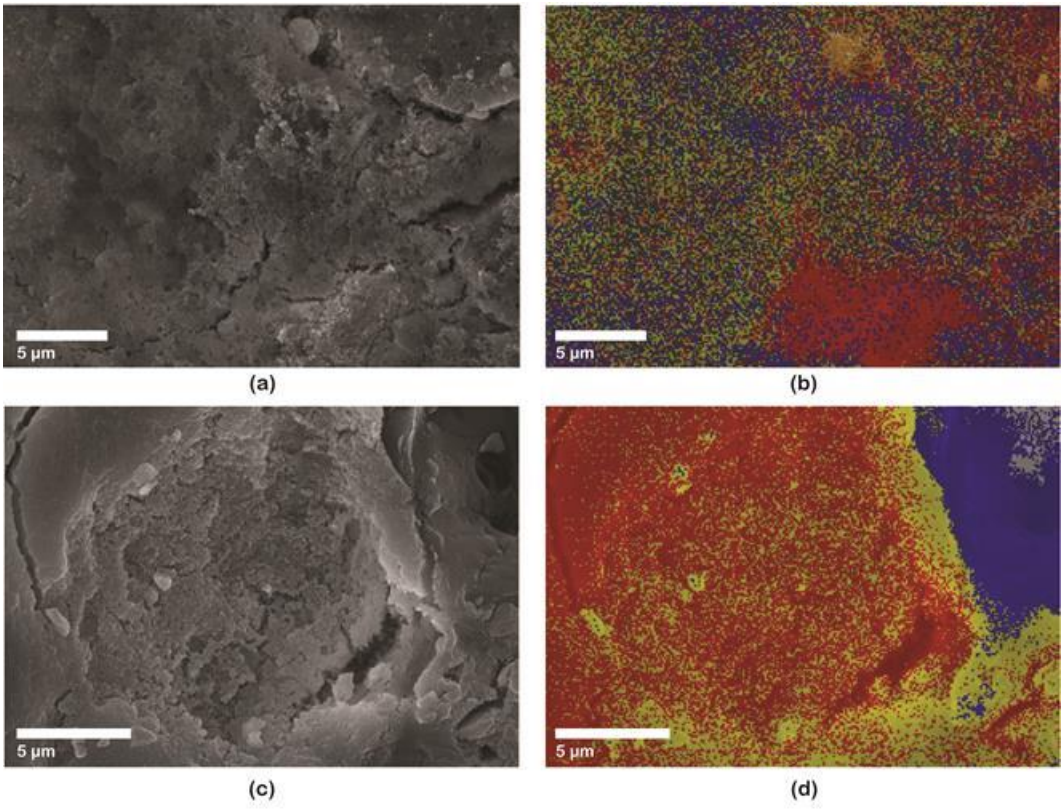

Figure 8 (a) – (b) SE micrograph and EDS element to phase map of Bindlas ash binder with approximate phase distributions of Na:Ca:Al:Si atomic % given by Red = 0.01:0.09:0.07:1 (unreacted silica particle); Yellow = 0.07:0.47:0.22:1 (reaction product); Blue = 0.07:0.28:0.23:1 (reaction product); Green = 0.10:0.43:0.24:1 (reaction product); Orange = 50% Carbon, and (c) – (d) SE micrograph and EDS element to phase map of Silverton ash binder with approximate Na:Ca:Al:Si atomic % distributions given by Red = 0:0.12:0:1 (reaction product); Yellow = 0.04:0.17:0.01:1 (reaction product); Blue = 88% Carbon

Conclusions

In this study, a biomass ash binder was formulated from ash (used as received), clay and hydrated lime using 2M NaOH as the activator. The binders prepared with two types of ashes achieved compressive strengths in range of 10–14 MPa after 28 days of curing at 30°C. Almost 50% of 28-day strength was achieved in the first 24 hours and a strong correlation between

compaction pressure and compressive strength indicated the influence of packing density on strength up to around 22 MPa.

The extent of dissolution of ashes could be correlated to the degree of amorphousness. The ash with higher amorphous content released higher amounts of [Si] into solution and the dissolution rate of both ashes decreased with time. Clay, which had significantly lower amorphous content, released an order of magnitude lower amount of [Si] than both types of ashes. The reaction between the hydrated lime and dissolved [Si] resulted in the formation of aluminum-substituted calcium silicate hydrate gel which was identified as the main reaction product in biomass ash binder formulated in this study. The morphology of the reaction product appeared to be globular and the ash with higher amorphous content led to a denser reaction product with higher surface area.

The study shows that biomass ash can be valorized into a cementitious binder using near-ambient temperature curing (30°C) and activators of low alkalinity (2M). The amorphous content of biomass ash governs the reactivity, and thereby, the strength development.

Acknowledgements

We would like to acknowledge the financial support for this research through the Tata Center for Technology and Design at Massachusetts Institute of Technology (MIT), Cambridge. The authors thank Mr. Pankaj Agrawal of Bindlas Duplux LTD. (Muzaffarnagar, India) for providing the materials used in this study. This work made use of the MRSEC Shared Experimental Facilities at MIT, supported by the National Science Foundation under award number DMR-1419807, and facilities at the Institute for Soldier Nanotechnologies (ISN) at MIT. We also acknowledge the research contributions of Samuel Wilson, Patrick Boisvert, Charlie Settens, Timothy McClure, Stephen Rudolph, and Wyoming Analytical Laboratories, Inc. This paper is

dedicated to the memory of Professor Hamlin Jennings, pioneer in cement science (1946-2015), his coauthors are grateful for his wisdom, enthusiasm and guidance.

References

[1] International Energy Agency, Key world energy statistics, Statistics (Ber). (2016) 80.

[2] J.M.O. Scurlock, D.O. Hall, The contribution of biomass to global energy use (1987), Biomass. 21 (1990) 75–81.

[3] International Energy Agency, World Energy Outlook 2010, 2010.

[4] U.S. Energy Information Administration, Annual Energy Outlook 2015, Off. Integr. Int. Energy Anal. 1 (2015) 1–244.

[5] E. Hughes, Biomass cofiring: Economics, policy and opportunities, Biomass and Bioenergy. 19 (2000) 457–465.

[6] IRENA, Renewable Power Generation Costs in 2014, (2015) 92. http://www.irena.org/DocumentDownloads/Publications/IRENA_RE_Power_Costs_2014_report.pdf.

[7] S. V. Vassilev, D. Baxter, L.K. Andersen, C.G. Vassileva, An overview of the chemical composition of biomass, Fuel. 89 (2010) 913–933.

[8] S. V. Vassilev, D. Baxter, C.G. Vassileva, An overview of the behaviour of biomass during combustion: Part II. Ash fusion and ash formation mechanisms of biomass types, Fuel. 117 (2014) 152–183.

[9] S. Detphan, P. Chindaprasirt, Prepration of fly ash and rice husk ash geopolymer, Int. J. Miner. Metall. Mater. 16 (2009) 720–726.

[10] S.A. Bernal, E.D. Rodríguez, R.M. de Gutiérrez, J. L. Provis, S. Delvasto, Activation of metakaolin/slag blends using alkaline solutions based on chemically modified silica fume and rice husk ash, Waste and Biomass Valorization. 3 (2012) 99–108.

[11] V. N. Castaldelli, J. L. Akasaki, J. L. P Melges, M. M. Tashima, L. Soriano, M. V. Borrachero, J. Monzó, J. Payá. Use of slag/sugar cane bagasse ash (SCBA) blends in the production of alkali-activated materials, Mater. 6 (2013) 3108–3127.

[12] M.S. Imbabi, C. Carrigan, S. McKenna, Trends and developments in green cement and concrete technology, Int. J. Sustain. Built Environ. 1 (2012) 194–216.

[13] J. Davidovits, Geopolymers, J. Therm. Anal. 37 (1991) 1633–1656.

[14] C. Shi, R. L. Day, Acceleration of the reactivity of fly ash by chemical activation, Cem. Concr. Res. 25 (1995) 15-21.

[15] A. Palomo, M.T. Blanco-Varela, M.L. Granizo, F. Puertas, T. Vazquez, M.W. Grutzeck, Chemical stability of cementitious materials based on metakaolin, Cem. Concr. Res. 29 (1999) 997–1004.

[16] P. Duxson, A. Fernández-Jiménez, J.L. Provis, G.C. Lukey, A. Palomo, J.S.J. van Deventer, Geopolymer technology: the current state of the art, J. Mater. Sci. 42 (2007) 2917–2933.

[17] G. Habert, J.B. D'Espinose De Lacaillerie, N. Roussel, An environmental evaluation of geopolymer based concrete production: Reviewing current research trends, J. Clean. Prod. 19 (2011) 1229–1238.

[18] E. Worrell, L. Price, N. Martin, C. Hendriks, L.O. Meida, Carbon dioxide emissions from the global cement industry, Annu. Rev. Energy Environ. 26 (2001) 303–329.

[19] L. Barcelo, J. Kline, G. Walenta, E. Gartner, Cement and carbon emissions, Mater. Struct. 47 (2014) 1055–1065.

[20] R. Rajamma, J.A. Labrincha, V.M. Ferreira, Alkali activation of biomass fly ash-metakaolin blends, Fuel. 98 (2012) 265–271.

[21] C.R. Shearer, J.L. Provis, S.A. Bernal, K.E. Kurtis, Alkali-activation potential of biomass-coal co-fired fly ash, Cem. Concr. Compos. 73 (2016) 62–74.

[22] N.N.N. Yeboah, C.R. Shearer, S.E. Burns, K.E. Kurtis, Characterization of biomass and high carbon content coal ash for productive reuse applications, Fuel. 116 (2014) 438–447.

[23] http://www.fao.org/faostat/en/#data/QC (Retrieved on Dec 26, 2016)

[24] K. Umamaheswaran, V.S. Batra, Physico-chemical characterisation of Indian biomass ashes, Fuel. 87 (2008) 628–638.

[25] S. V. Vassilev, D. Baxter, C.G. Vassileva, An overview of the behaviour of biomass during combustion: Part I. Phase-mineral transformations of organic and inorganic matter, Fuel. 112 (2013) 391–449.

[26] L.L. Baxter, T.R. Miles, T.R. Miles Jr, B.M. Jenkins, T. Milne, D. Dayton, R.W. Bryers, L.L. Oden, The behavior of inorganic material in biomass-fired power boilers: field and laboratory experiences, Fuel Process. Technol. 54 (1998) 32.

[27] A. Hajimohammadi, J.S.J. van Deventer, Dissolution behaviour of source materials for synthesis of geopolymer binders: A kinetic approach, Int. J. Miner. Process. 153 (2016) 80–86.

[28] S. Chandrasekhar, P.N. Pramada, J. Majeed, Effect of calcination temperature and heating rate on the optical properties and reactivity of rice husk ash, J. Mater. Sci. 41 (2006) 7926–7933.

[29] G.C. Cordeiro, R.D. Toledo Filho, E.M.R. Fairbairn, Effect of calcination temperature on the pozzolanic activity of sugar cane bagasse ash, Constr. Build. Mater. 23 (2009) 3301–3303.

[30] J. James, M. Subba Rao, Reaction product of lime and silica from rice husk ash, Cem. Concr. Res. 16 (1986) 67–73.

[31] G.C. Cordeiro, R.D. Toledo Filho, L.M. Tavares, E.M.R. Fairbairn, Pozzolanic activity and filler effect of sugar cane bagasse ash in Portland cement and lime mortars, Cem. Concr. Compos. 30 (2008) 410–418.

[32] S. Kumar, and R. Kumar. Mechanical Activation of Fly Ash: Effect on Reaction, Structure and Properties of Resulting Geopolymer. Ceramics International 37 (2011) 533–41.

[33] T. Poinot, M.E. Laracy, C. Aponte, H. Jennings, J.A. Ochsendorf, E.A. Olivetti, Beneficial Use of Boiler Ash in Alkali-Activated Bricks, Res. Cons. Recycl. In press.

[34] http://education.afpm.org/refining/petroleum-coke/ (Retrieved on Sept 19, 2017)

[35] H.M. Rietveld, A profile refinement method for nuclear and magnetic structures, J. Appl. Crystallogr. 2 (1969) 65–71.

[36] J. He, J. Zhang, Y. Yu, G. Zhang, The strength and microstructure of two geopolymers derived from metakaolin and red mud-fly ash admixture: A comparative study, Constr. Build. Mater. 30 (2012) 80–91.

[37] E.H. Oelkers, J. Schott, J.-L.L. Devidal, The effect of aluminum, pH, and chemical affinity on the rates of aluminosilicate dissolution reactions, Geochim. Cosmochim. Acta. 58 (1994) 2011–2024.

[38] X. Cong, R.J. Kirkpatrick, 29Si MAS NMR study of the structure of calcium silicate hydrate, Adv. Cem. Based Mater. 3 (1996) 144–156.

[39] B. Lothenbach, K. Scrivener, R.D.D. Hooton, Supplementary cementitious materials, Cem. Concr. Res. 41 (2011) 1244–1256.

[40] S.D. Wang, K.L. Scrivener, Hydration products of alkali activated slag cement, Cem. Concr. Res. 25 (1995) 561–571.

[41] A. Brough, A. Atkinson, Sodium silicate-based, alkali-activated slag mortars: Part I. Strength, hydration and microstructure, Cem. Concr. Res. 32 (2002) 865–879.

[42] D. Ravikumar, S. Peethamparan, N. Neithalath, Structure and strength of NaOH activated concretes containing fly ash or GGBFS as the sole binder, Cem. Concr. Compos. 32 (2010) 399-410.

[43] I. Ismail, S.A. Bernal, J.L. Provis, R. San Nicolas, S. Hamdan, J.S.J.J. van Deventer, Modification of phase evolution in alkali-activated blast furnace slag by the incorporation of fly ash, Cem. Concr. Compos. 45 (2014) 125–135.

[44] H.F.W. Taylor, Cement Chemistry, Thomas Telford, 2nd Edition, (1997).

[45] W.A. Hunnicutt, Characterization of calcium-silicate-hydrate and calcium-alumino-silicate-hydrate, MS Thesis, University of Illinois at Urbana-Champaign, 2013.

[46] R.J. Myers, E. L'Hopital, J.L. Provis, B. Lothenbach, Composition-solubility-structure relationships in calcium (alkali) aluminosilicate hydrate (C-(N,K-)A-S-H), Dalt. Trans. 44 (2015) 13530–13544.

[47] M. Daugaard Andersen, H.J. Jakobsen, Jø. Skibsted, Incorporation of aluminum in the calcium silicate hydrate (C-S-H) of hydrated Portland cements: A high-field 27Al and 29Si MAS NMR investigation, Inorg. Chem. 42 (2003) 2280–2287.

[48] I. Garcia-Lodeiro, A. Palomo, A. Fernández-Jiménez, D.E. Macphee, Compatibility studies between N-A-S-H and C-A-S-H gels. Study in the ternary diagram Na_2O–CaO–Al_2O_3–SiO_2–H_2O, Cem. Concr. Res. 41 (2011) 923–931.

[49] M.C. Garci Juenger, H.M. Jennings, The use of nitrogen adsorption to assess the

microstructure of cement paste, Cem. Concr. Res. 31 (2001) 883–892.

[50] P. Duxson, J.L. Provis, G.C. Lukey, S.W. Mallicoat, W.M. Kriven, J.S.J. Van Deventer, Understanding the relationship between geopolymer composition, microstructure and mechanical properties, Colloids Surfaces A Physicochem. Eng. Asp. 269 (2005) 47–58.

[51] J.J. Thomas, H.M. Jennings, A.J. Allen, The Surface Area of Cement Paste As Measured By Neutron: Evidence for Two C-S-H Morphologies, Cem. Concr. Res. 28 (1998) 897–905.

[52] Q. Zeng, D. Zhang, H. Sun, K. Li, Characterizing pore structure of cement blend pastes using water vapor sorption analysis, Mater. Charact. 95 (2014) 72–84.

[53] C.K. Yip, G.C. Lukey, J.S.J. van Deventer, The coexistence of geopolymeric gel and calcium silicate hydrate at the early stage of alkaline activation, Cem. Concr. Res. 35 (2005) 1688–1697.